Space Weather

RESEARCH ARTICLE
10.1029/2020SW002655

Markov Chain-Based Stochastic Modeling of Deep Signal Fading: Availability Assessment of Dual-Frequency GNSS-Based Aviation Under Ionospheric Scintillation

Andrew K. Sun[1], Hyeyeon Chang[1], Sam Pullen[2], Hyosub Kil[3], Jiwon Seo[4], Y. Jade Morton[5], and Jiyun Lee[1]

[1]Korea Advanced Institute of Science and Technology, Daejeon, Republic of Korea, [2]Stanford University, Stanford, CA, USA, [3]The Johns Hopkins University Applied Physics Laboratory, Laurel, MD, USA, [4]Yonsei University, Incheon, Republic of Korea, [5]University of Colorado Boulder, Boulder, CO, USA

Abstract Deep signal fading due to ionospheric scintillation severely impacts global navigation satellite system (GNSS)-based applications. GNSS receivers run the risk of signal loss under deep fading, which directly leads to a significant decrease in navigation availability. The impact of scintillation on GNSS-based applications can be mitigated via dual-frequency signals which provide a backup channel. However, the benefit of dual-frequency diversity highly depends on the correlation of fading processes between signals at different frequencies. This paper proposes a Markov chain-based model that simulates the actual behavior of correlated fading processes in dual-frequency channels. A set of recorded scintillation data was used to capture transitions among all fading states based on the fading and recovery of each signal frequency. A statistical study of deep fading characteristics in this data revealed that the Markov chain-based model accurately generates realistic correlated fading processes. Using the proposed model, aviation availability of localizer performance with vertical guidance down to a 200-foot decision height ("LPV-200") under a strong scintillation scenario is analyzed by considering the effects of signal outages due to deep fading. A parametric analysis of the availability resulting from variations in mean time to loss of lock, mean time to reacquisition, and ionospheric delay uncertainty was conducted to investigate the performance standards on GNSS-based aviation under scintillation. The analysis results demonstrate a significant benefit of frequency diversity on aviation availability during scintillation. This model will further enable the assessment of GNSS-based availability for aviation and other applications under a full range of scintillation conditions.

Plain Language Summary One of the most detrimental impacts of space weather on GNSS-based navigation applications is ionospheric scintillation in equatorial region, which can cause deep and frequent signal fading on GNSS signals. In particular, GNSS navigation may be lost when multiple satellites are briefly unusable for GNSS receiver calculations due to the signal fades caused by scintillation. The use of dual-frequency signals can diminish the impact of scintillation by providing a backup ranging source on one frequency. However, frequency diversity is only partially helpful because the effect of scintillation is correlated across frequencies, meaning that a receiver may still lose satellites when their signals on both frequencies are simultaneously plagued by deep fading. Here we propose a new stochastic model to represent a more accurate description of correlated fading processes observed in actual scintillation data. We incorporate scintillation effects into a simulation of aviation availability. The simulation results provide estimates of the impact of scintillation on L1 single and L1/L5 dual-frequency aviation availability and quantify the benefit from the use of dual-frequency signals during strong scintillation. Further development of this model will enable the assessment of effects from other scintillation conditions and scenarios on availability for aviation and other applications of GNSS.

Key Points:

- Deep fades observed in a Global Positioning System (GPS) L1/L5 strong scintillation data set have been characterized in terms of availability for global navigation satellite system (GNSS) navigation
- A stochastic model based on a Markov chain accurately generates realistic correlated fading processes of GNSS signals under scintillation
- New Markov chain model confirms that use of dual-frequency GNSS signals significantly enhances aviation availability during scintillation

Correspondence to:
J. Lee,
jiyunlee@kaist.ac.kr

Citation:
Sun, A. K., Chang, H., Pullen, S., Kil, H., Seo, J., Morton, Y. J., & Lee, J. (2021). Markov chain-based stochastic modeling of deep signal fading: Availability assessment of dual-frequency GNSS-based aviation under ionospheric scintillation. *Space Weather*, *19*, e2020SW002655. https://doi.org/10.1029/2020SW002655

Received 10 OCT 2020
Accepted 13 JUN 2021

1. Introduction

Various space weather effects adversely impact global navigation satellite system (GNSS)-based applications. One of the most adverse space weather effects is ionospheric scintillation, which results in rapid fluctuations in the amplitude and phase of GNSS signals. This is caused by refractive and/or diffractive wave interference when signals pass through small-scale irregular structures in the ionosphere (Kintner

et al., 2007). GNSS signals experience deep and frequent fading during strong scintillation, which in turn places additional stress on the tracking loops in GNSS receivers. As its severity increases, deep signal fading leads to cycle slips or losses of lock in the receiver's carrier tracking loop (Breitsch et al., 2020; Humphreys et al., 2010; Skone et al., 2001; see also Knight, 2000). When GNSS signals from multiple satellites are simultaneously plagued by deep fading, the receiver may lose more than one satellite-tracking channel, leading to a loss of navigation availability for GNSS-based applications (Lee et al., 2017; Seo et al., 2009).

Scintillation effects can be alleviated by dual-frequency broadcasts from more recent generations of GNSS satellites. The Global Positioning System (GPS) has launched a number of new satellites since 2010 that broadcast two frequencies in aeronautical bands designated as L1 (1,575.42 MHz) and L5 (1,176.45 MHz). Both of these frequencies are within aeronautical radio navigation service (ARNS) frequency bands, which is intended for civil aviation operations (FAA, 2010). Following existing single-frequency GPS L1-based aviation systems, the development of dual-frequency GPS L1/L5-based systems for aviation operations is ongoing (Felux et al., 2017; Gerbeth et al., 2016; Walter et al., 2012). Furthermore, the worldwide development of GNSS constellations, including GLONASS, Galileo, and BeiDou is in progress to provide a sufficient number of satellites that transmit dual-frequency signals in both L1/E1 and L5/E5 frequency bands for civil aviation users (ICAO, 2018). Since dual-frequency GNSS avionics can independently track both signals in different frequency bands, they can provide a backup channel when a signal on one frequency is briefly lost due to deep fading. This frequency diversity enables aviation receivers to maintain tracking as much as possible on at least one signal and thus mitigate the scintillation impact on GNSS-based aviation operations.

To assess the benefit of dual-frequency GNSS under scintillation, the degree of correlation of deep fades across frequency bands must be addressed. A high degree of correlation of deep fades (or signal intensity) between different frequency bands leads to a higher probability of concurrent deep fading on both frequency bands (potentially leading to complete loss of the affected satellite), which may directly reduce the availability of GNSS-based aviation. Previous studies have investigated the level of signal intensity correlation across frequency bands under scintillation. Carrano et al. (2012) demonstrated a marked decrease in signal intensity correlation between different frequency bands as the scintillation severity increases. Jiao et al. (2016) showed a low percentage of concurrent deep fading on multiple frequency bands, indicating that at least one frequency band is at a normal intensity level most of the time. This lower correlation of signal intensity across frequency bands provides an advantage from dual-frequency tracking during strong scintillation. However, the remaining correlation of deep fades still impacts availability to some degree. Thus, the degree of correlation must be accurately quantified to assess the impact of scintillation on the availability of dual-frequency GNSS-based applications.

Seo and Walter (2014) investigated possible improvements in the availability of GNSS-based aviation under strong scintillation when dual-frequency signals are available. This study utilized the Poisson process-based fading process model proposed in Seo et al. (2011b), which uses an arbitrary rate and correlation level of deep fades between different frequency channels to generate independent Poisson processes of single-frequency-only and dual-frequency-concurrent deep fading. However, since scintillation data for GPS L5 was not available at the time, the fading rate of the L5 frequency and the correlation between L1 and L5 frequencies were arbitrarily assumed instead of being based on actual scintillation data. Sun et al. (2020) recently proposed an improved model based on statistics of observed GPS L1/L5 scintillation data. However, this model has a significant limitation due to the independent generation of each single-frequency-only and dual-frequency-concurrent fading process. This prevents the model from describing fading processes in dual-frequency channels with an accurate measure of their temporal correlation.

In response, this paper proposes a new model to provide a better description of correlated fading processes in dual-frequency GNSS signals. The model employs a Markov chain by representing transitions in four fading states: No fading, L1-only fading, L5-only fading, and L1/L5-concurrent fading. The fading process for each GPS satellite is expressed through a Markov chain with stationary conditional probabilities based on the Poisson rate parameters of all state transitions: Rate of fading onset or recovery for each frequency. In this model, the temporal correlation of deep fades across frequency bands is addressed by applying different transition parameters depending on the current fading state. This capability allows the model to better capture the actual behavior of a correlated fading process as part of an analysis of availability of GNSS-based applications under various scintillation environments.

The objective of this paper is to assess the benefit of dual-frequency GNSS avionics under strong scintillation by providing an accurate description of correlated fading processes using the Markov chain-based fading process model. A set of actual scintillation data is used in this study to estimate the modeling parameters, and a description of this data set is presented in Section 2. Section 3 presents an analysis method to define and characterize deep fading from the perspective of GNSS-based navigation availability. Time between fading onsets and fading duration are investigated because they are two important characteristics which directly affect navigation availability. Sections 4.1 and 4.2 include a brief review of the Poisson process-based model in Sun et al. (2020) to generate fading processes in dual-frequency channels along with a full description of our newly proposed Markov chain-based model. In Section 4.3, the characteristics of deep fades generated from the Poisson process-based model and the Markov chain-based model are compared with those from real scintillation data to evaluate the statistical accuracy of the fading process models. In Section 5, an availability simulation of GNSS-based aviation operations is implemented under the strong scintillation scenario generated from the proposed fading process model. In Section 6, the paper is summarized and future works are suggested.

2. Equatorial Scintillation Data Set

Ionospheric scintillation occurs most frequently and severely in the equatorial region, and its effect is typically the greatest at solar maximum (Basu et al., 1988). Especially during the post-sunset and pre-midnight periods, an enhanced eastward electric field (called pre-reversal enhancement) often develops in the equatorial ionosphere and uplifts the *F* region altitude, providing the preferential condition for the formation of irregular structures called equatorial plasma bubbles (EPBs) (Fejer et al., 1999; Hysell et al., 1990; Kelley et al., 1981; Kil et al., 2009; Ott, 1978; Woodman, 1970). Inside an EPB structure, the density of ionospheric plasma is significantly lower than in the surrounding ionosphere, and the spatial inhomogeneities of the refractive index produce refractive/diffractive scattering to cause ionospheric scintillation (ITU, 2013; Yeh & Liu, 1982).

The scintillation study presented here is based on GPS L1/L5 dual-frequency measurements collected in Hong Kong (22.3°N, 114.2°E) (Jiao et al., 2015; Morton et al., 2015). This site is located near the crest of the equatorial ionization anomaly (EIA) (around magnetic latitude ±15°), where strong and frequent scintillation tends to occur (Basu et al., 2002; Kintner et al., 2007). At this site, a Septentrio PolaRxS Pro ionospheric scintillation monitoring (ISM) receiver was configured to output raw signal intensity measurements at a rate of 50 Hz on multiple GNSS frequency bands. The most severe scintillation period was selected based on the S_4 index shown in Figure 1a. The selected period was from 13:46:00 to 14:16:00 UTC (from 21:46:00 to 22:16:00 LT) on March 2, 2014, which was near the maximum of the previous solar cycle 24. The S_4 index is a measure of amplitude scintillation and is defined as the normalized (and thus unitless) standard deviation of the detrended signal intensity. In this study, the S_4 index was corrected by removing the effects of ambient noise as explained by Van Dierendonck et al. (1993). During the selected period, the S_4 index around or exceeding unity lasted for approximately 30 min when the satellite was at elevation angles above 20°, which indicates strong scintillation. Detrended signal intensity measurements (explained in Section 3.1) in Figure 1b also show strong scintillation effects over this period with repeated frequent and deep signal fades.

The ionospheric conditions around the time of the scintillation measurements at Hong Kong were investigated using satellite observations. Figure 2a shows the airglow image of the atomic oxygen (OI) 135.6 nm emission observed by the Special Sensor Ultraviolet Spectrographic Imager (SSUSI) (Paxton et al., 2017) on board the Defense Meteorological Satellite Program (DMSP) F18 satellite. Figure 2a is the stack of the SSUSI disk-scan projected to an ionospheric *F* region peak density altitude of 350 km. The OI 135.6 nm emission at night is produced by radiative recombination of oxygen ions in the ionosphere. Because oxygen ions are the main constituent of the ionospheric *F* region, the intensity of the OI 135.6 nm emission observed by SSUSI is a good representation of the line-of-sight integral of the electron density up to the satellite's altitude. DMSP F18 has a sun-synchronous circular orbit at an altitude of 840 km with an orbital inclination of 98°. EPBs appear as the emission depletion bands shown in Figure 2a. In these bands, oxygen ion density is smaller than ambient. Although we cannot identify EPBs around Hong Kong because it is outside the SSUSI swath, EPBs detected in the magnetic south would also appear in the magnetic north because of their

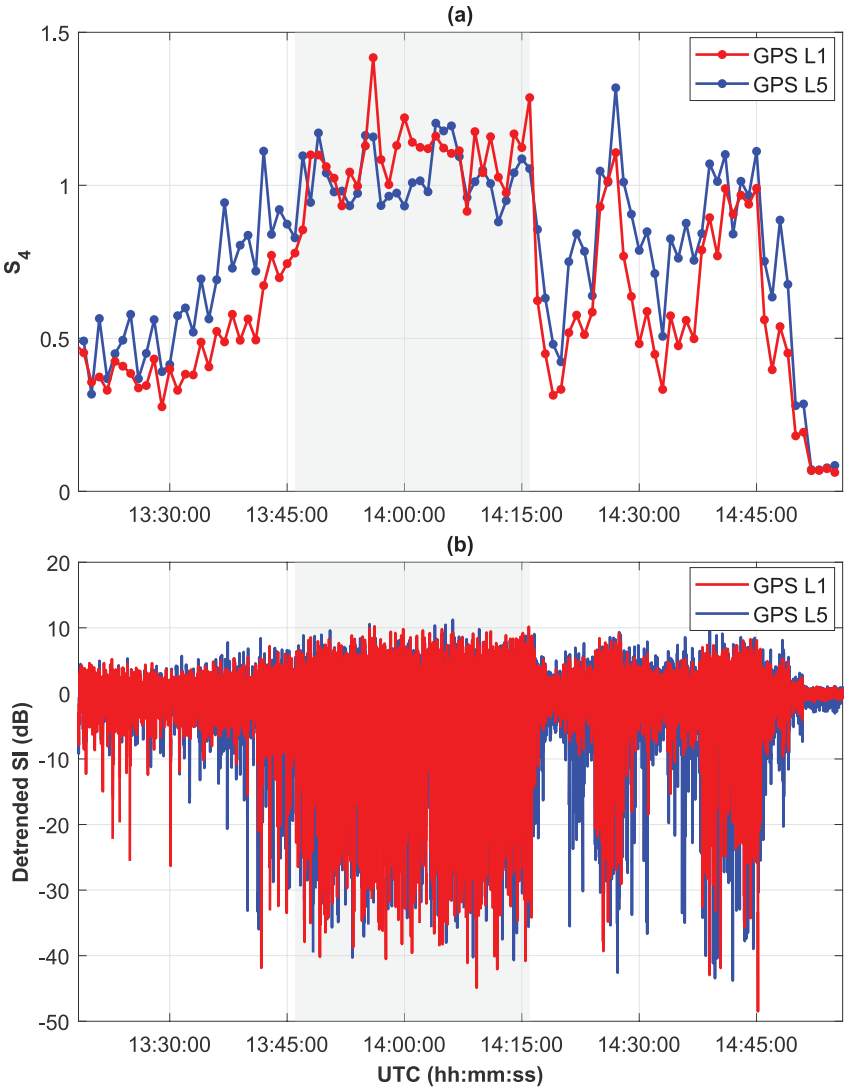

Figure 1. (a) S4 index and (b) detrended signal intensity measurements of Global Positioning System (GPS) L1/L5 dual-frequency signals on PRN 01, collected from Hong Kong on March 2, 2014. The gray shaded area depicts the strong scintillation period selected for analysis in this paper.

magnetic conjugacy with respect to the magnetic equator (Kelley et al., 2003; Kil et al., 2009). EPBs are not distinguishable near the magnetic equator due to low background intensity (or low oxygen ion density).

Figure 2b presents the ion density observed by the Coupled Ion-Neutral Dynamics Investigation (CINDI) instrument on board the Communication/Navigation Outage Forecasting System (C/NOFS) satellite. The yellow line in Figure 2a shows the ground track of C/NOFS around the selected period on March 2, 2014. Density depletions accompanied by irregular structures are EPBs. Thus, EPBs have developed at the longitude around Hong Kong and at the magnetic north and are therefore the most likely cause of scintillations detected at Hong Kong.

3. Deep Fading Analysis

3.1. Deep Fading Definition

Deep signal fading is defined as an event in which the received signal intensity drops below a threshold that is low enough to break a receiver's carrier tracking loop and cause loss of lock on the signal (Seo et al., 2009).

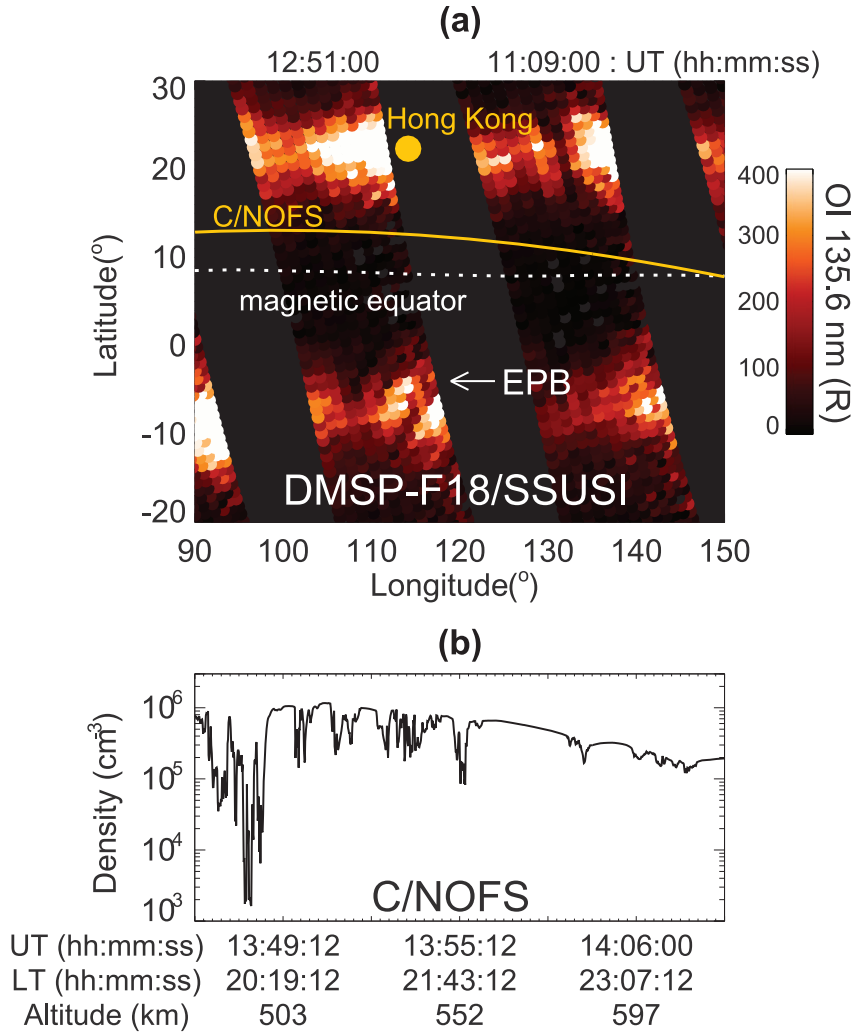

Figure 2. Detection of equatorial plasma bubbles (EPBs) at the longitude of Hong Kong on March 2, 2014. (a) Composite image of the OI 135.6 nm emission observed by DMSP F18-SSUSI. The DMSP F18 orbit was moving from south to north in a sun-synchronous orbit, and the local solar time when the satellite passed the geographic equator was ~20 h. (b) Measurement of the ion density by C/NOFS-CINDI.

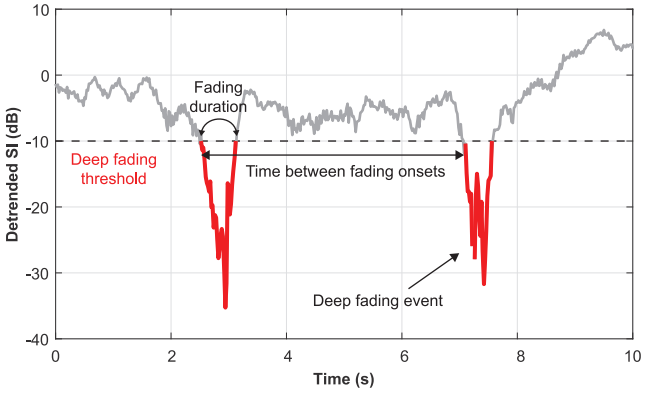

Figure 3. Illustration of deep fading events and their characteristics (time between fading onsets and fading duration) extracted from detrended signal intensity measurements with a threshold of −10 dB.

To determine signal fading, the raw signal intensity was detrended using a moving average filter over a 60 s interval to remove low-frequency contributions from satellite-receiver range variations, antenna patterns, as well as background ionospheric and tropospheric delays (Van Dierendonck & Arbesser-Rastburg, 2004). A threshold of −10 dB was used to define and extract deep fading events on both L1 and L5 frequency channels within their detrended signal intensities as shown in Figure 3. Deep fading events that were separated by less than a certain time interval (0.06 s in this study) were merged into a single event to include undetected samples near the threshold due to measurement noise.

3.2. Deep Fading Characteristics

To analyze the effects of deep signal fading on the navigation performance of GNSS-based applications, two quantities were characterized in this study: Time between fading onsets and fading duration, as shown in

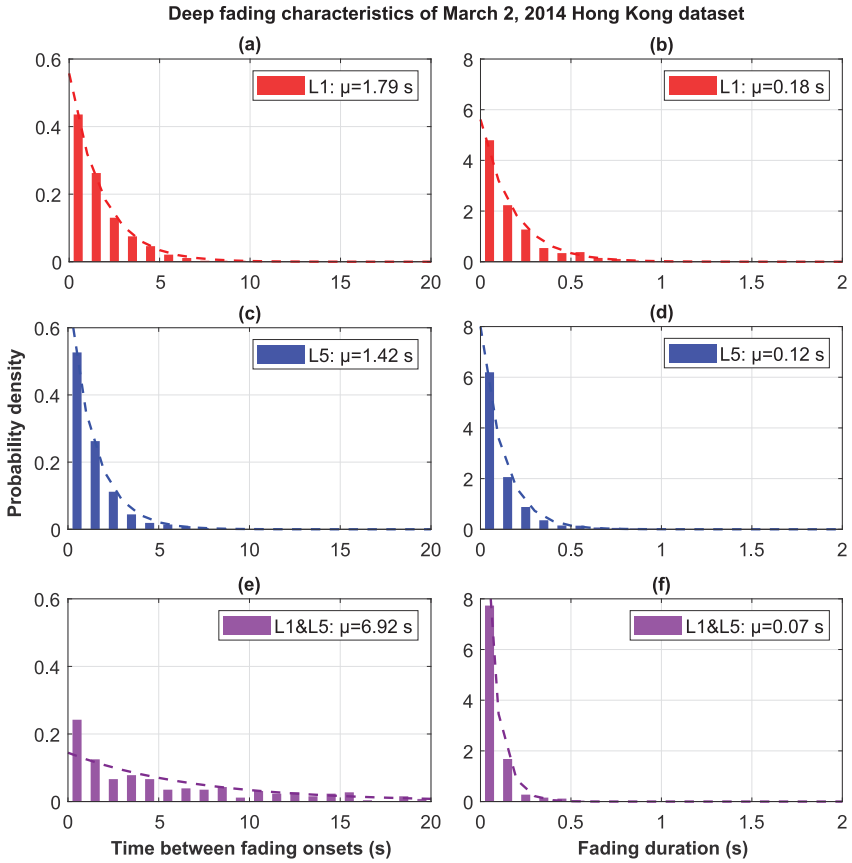

Figure 4. Normalized histograms of time between fading onsets and fading duration for (a) and (b) Global Positioning System (GPS) L1 (c) and (d) L5 and (e) and (f) L1/L5-concurrent deep fading obtained from the March 2, 2014 Hong Kong data set. The normalized histograms are fitted into exponential distributions of their corresponding rates, which were estimated using the reciprocals of the mean time between fading onsets and fading duration, respectively.

Figure 3. Time between fading onsets is defined as the time difference between onsets of adjacent fading events whose detrended signal intensities drop below the threshold. Note that shorter time between fading onsets may disrupt the continuity of GNSS navigation due to satellite geometry loss when signal losses occur under deep fading. Time between fading onsets is also related to the effective carrier smoothing time of the aviation receiver. The smoothing filter must continuously operate for more than a certain time window without any losses of lock or cycle slips to attenuate the code noise down to its steady-state level (Seo et al., 2009, 2011a). Hence, frequent loss of lock due to short time between fading onsets results in frequent resets of the smoothing filter, preventing it from reducing the code noise to its desired level.

The other important characteristic is fading duration, which is the time interval during which the detrended signal intensity remains below the threshold. An increase in fading duration increases the chance of a receiver channel losing lock, provided that the fading depth is near or below the threshold of the tracking loop (Knight, 2000). The distribution of fading duration varies significantly depending on the threshold of fading depth, as explained in the fading duration model presented in Seo et al. (2009). The reacquisition time of a receiver depends on its tracking threshold and required coasting time. A receiver can reacquire a signal after recovering the signal intensity above the tracking threshold; therefore, the fading duration is an important parameter for the reacquisition capability of receivers.

Figure 4 shows normalized histograms obtained by estimating the probability density functions (i.e., the sum over all bin areas is 1) of the deep fading characteristics from the March 2, 2014 Hong Kong data set: Time between fading onsets and fading duration of GPS L1 (Figures 4a and 4b), L5 (Figures 4c and 4d), and their concurrent deep fading (Figures 4e and 4f). The normalized histograms of both characteristics were fitted into exponential distributions with their corresponding rates, which were estimated using the

reciprocals of mean time between fading onsets and fading duration, respectively (Sun et al., 2020). It can be seen that more frequent deep fades (with shorter time between fading onsets) occur in the L5 signal (Figure 4c) than in the L1 signal (Figure 4a). This demonstrates the dependence of scintillation on frequency, where lower frequency bands are more vulnerable (Ogawa et al., 1980). L1 and L5 concurrent deep fading is defined by overlaps between deep fades in the L1 and L5 dual-frequency channels. Note that the characteristics of concurrent deep fading are the most important indicators of the scintillation impact on dual-frequency operation of GNSS navigation.

4. Methods to Generate Correlated Fading Processes

4.1. Poisson Process-Based Model

A method to simulate correlated fading processes was proposed in Seo et al. (2011b) to assess the impact of scintillation on GNSS-based navigation availability. This method was based on the observation that the distribution of time between deep fades (or time between fading onsets in our definition) during scintillation approximately follows an exponential distribution (Seo et al., 2011b). This implies that the counting process of the number of deep fades can be modeled as a Poisson process. A Poisson process is defined as an independent counting process $\left\{N\left(t\right)=1,2,3,\cdots;t\geq 0\right\}$ in which the probabilities of any number of events in an infinitesimal interval $\left(t,t+\delta\right]$ satisfy:

$$\text{Prob}\left\{N\left(t+\delta\right)-N\left(t\right)=0\right\}=e^{-\lambda\delta}=1-\lambda\delta+h\left(\delta^2\right) \tag{1}$$

$$\text{Prob}\left\{N\left(t+\delta\right)-N\left(t\right)=1\right\}=\lambda\delta e^{-\lambda\delta}=\lambda\delta+h\left(\delta^2\right) \tag{2}$$

$$\text{Prob}\left\{N\left(t+\delta\right)-N\left(t\right)\geq 2\right\}=h\left(\delta^2\right) \tag{3}$$

where λ is the rate parameter of the process, and $h\left(\delta^2\right)$ indicates higher order terms which can be neglected for small δ.

An alternate definition of a Poisson process is any counting process in which inter-arrival intervals T between events are independent and identically distributed (IID) exponential random variables, $T\sim\exp\left(\lambda\right)$, with the rate λ of the corresponding Poisson process (Gallager, 1996). Based on this equivalent definition of a Poisson process, a fading process can be simulated by generating exponentially distributed random variables of times between deep fades (or times between fading onsets) with the rate of the corresponding Poisson process that best fits the real scintillation data to be modeled.

To address the correlation of deep fades between different frequency channels, this method uses the superposition property of a Poisson process that the sum of independent Poisson processes also follows a Poisson process with the sum of their rates (Gallager, 1996). Suppose, that $\left\{N_{1,only}\left(t\right);t\geq 0\right\}$, $\left\{N_{5,only}\left(t\right);t\geq 0\right\}$, and $\left\{N_{15}\left(t\right);t\geq 0\right\}$ are independent Poisson processes of rates $\lambda_{1,only}$, $\lambda_{5,only}$ and λ_{15}, respectively. $\left\{N_{1,only}\left(t\right);t\geq 0\right\}$ and $\left\{N_{5,only}\left(t\right);t\geq 0\right\}$ are respective single-frequency-only fading processes of GPS L1 and L5 channels. $\left\{N_{15}\left(t\right);t\geq 0\right\}$ is a common fading process between the L1 and L5 channels, meaning that both signals are simultaneously fading or not. Then, as given in Equations 4 and 5, the sums of independent Poisson processes $\left\{N_{15}\left(t\right);t\geq 0\right\}$ with $\left\{N_{1,only}\left(t\right);t\geq 0\right\}$ and $\left\{N_{15}\left(t\right);t\geq 0\right\}$ with $\left\{N_{5,only}\left(t\right);t\geq 0\right\}$ result in Poisson processes $\left\{N_1\left(t\right);t\geq 0\right\}$ and $\left\{N_5\left(t\right);t\geq 0\right\}$ of rates $\lambda_{1,only}+\lambda_{15}$ and $\lambda_{5,only}+\lambda_{15}$, respectively:

$$N_1\left(t\right)=N_{1,only}\left(t\right)+N_{15}\left(t\right) \tag{4}$$

$$N_5\left(t\right)=N_{5,only}\left(t\right)+N_{15}\left(t\right) \tag{5}$$

The model in Sun et al. (2020) improves on this by additionally modeling fading duration (which also follows an exponential distribution) based on the March 2, 2014 Hong Kong data set. In this method, each

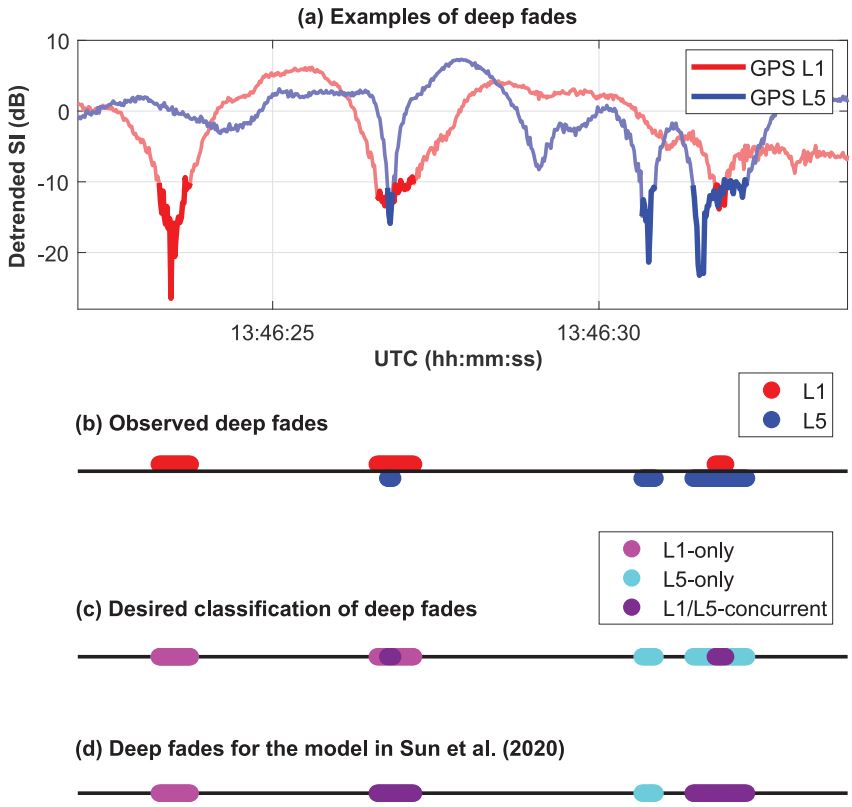

Figure 5. (a) and (b) Examples of deep fades in the Global Positioning System (GPS) L1/L5 dual-frequency channels for PRN 01 observed in the March 2, 2014 Hong Kong data set, (c) those with a desired classification of deep fading, and (d) the definition of deep fading in Sun et al. (2020).

fading process is represented by generating starting times of deep fades with the corresponding exponentially distributed random variable of time between fading onsets and independently generating their durations following the fading onsets with the corresponding exponentially distributed random variable of fading duration.

However, in the observation of deep fades in dual-frequency bands shown in Figure 5, overlapping deep fades resulted in consecutive sequences of L1-only, L5-only and L1/L5-concurrent deep fades (shown in Figure 5c). Such sequential behaviors of deep fades cannot be described by the superposition of their Poisson processes because each process is independently generated without modeling the correlated temporal structure between them. Due to this restriction, the model in Sun et al. (2020) defined new "concurrent" fading events by combining overlapping L1 and L5 deep fades into a single event which spans all of the combined fades, even if only part of the overlapping period includes concurrent deep fading (this is illustrated in Figure 5d). As a result, concurrent fading is common on both L1 and L5 channels.

Figure 6 shows the resulting parameters for the Poisson process-based model extracted from the March 2, 2014 Hong Kong data set. Although the definition of concurrent deep fading proposed in Sun et al. (2020) allows us to simplify the definition of fading processes to model them as independent Poisson processes, this yields very conservative results by providing much longer durations of concurrent deep fading (shown in Figure 6f) compared to that from the observed results (shown in Figure 4f) (e.g., 26.2% of the new-definition concurrent fades lasted longer than 0.5 s for the Poisson process-based model, compared to 3.9% in the observed results).

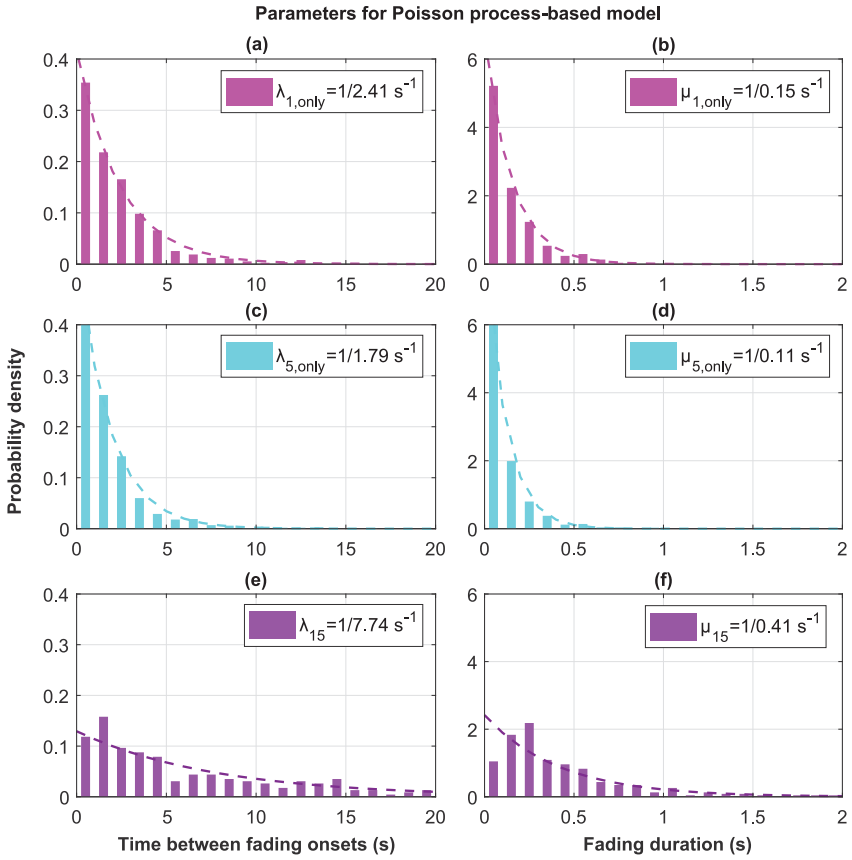

Figure 6. Parameters for the Poisson process-based model in Sun et al. (2020) extracted from the March 2, 2014 Hong Kong data set. Fading processes are generated in which the occurrence times of fading onset are exponentially distributed with rates of $\lambda_{1,only}$, $\lambda_{5,only}$ and λ_{15}, while fading durations are generated from exponentially distributed random variables with rates of $\mu_{1,only}$, $\mu_{5,only}$ and μ_{15}, respectively.

4.2. Markov Chain-Based Model

This section provides a new method based on the Markov chain concept to describe correlated deep fades in particular by including all possible transitions between fading states due to the onsets of fades and recoveries from fades of each signal frequency. Figure 7a shows the state-space diagram of the fading process model for dual-frequency channels. It assigns four fading states: 0 (no fading), 1 (L1-only fading), 5 (L5-only fading), and 15 (L1/L5-concurrent fading). The model was described as a stationary Markov chain, that is, all time intervals between state transitions are assumed to be exponentially distributed with constant rates; thus, all transitions satisfy the Markov property due to the memoryless property of the exponential distribution. Certain state transitions were not considered due to their improbability in very short time intervals. For example, direct transitions between states 0 and 15 are very rare since signals on the two frequencies are very unlikely to both fade or both recover from fades within the same time interval. Similarly, transitions between states 1 and 5 are very rare, as occurrences of L1 fading onset along with L5 fading recovery (or vice versa) are very unlikely within a single time interval. To avoid these improbable state transitions, we simplified the fading state sequences: One epoch of state 5 was inserted in between states 0 and 15, and one epoch of state 15 was inserted in between states 1 and 5.

Borrowing the concept of a Poisson process from Section 4.1, the counting process with IID exponentially distributed inter-arrival times is a Poisson process, which in turn means that the Markov chain-based model can be represented with state transitions governed by independent Poisson processes, generally called continuous-time Markov chains (Billinton & Allan, 1983; Gallager, 1996). Therefore, the probability of a state transition from state i to j for the Markov chain can be derived from Equations 1 to 3 in terms of the discretized form of a Poisson process of rate $q_{i,j}$,

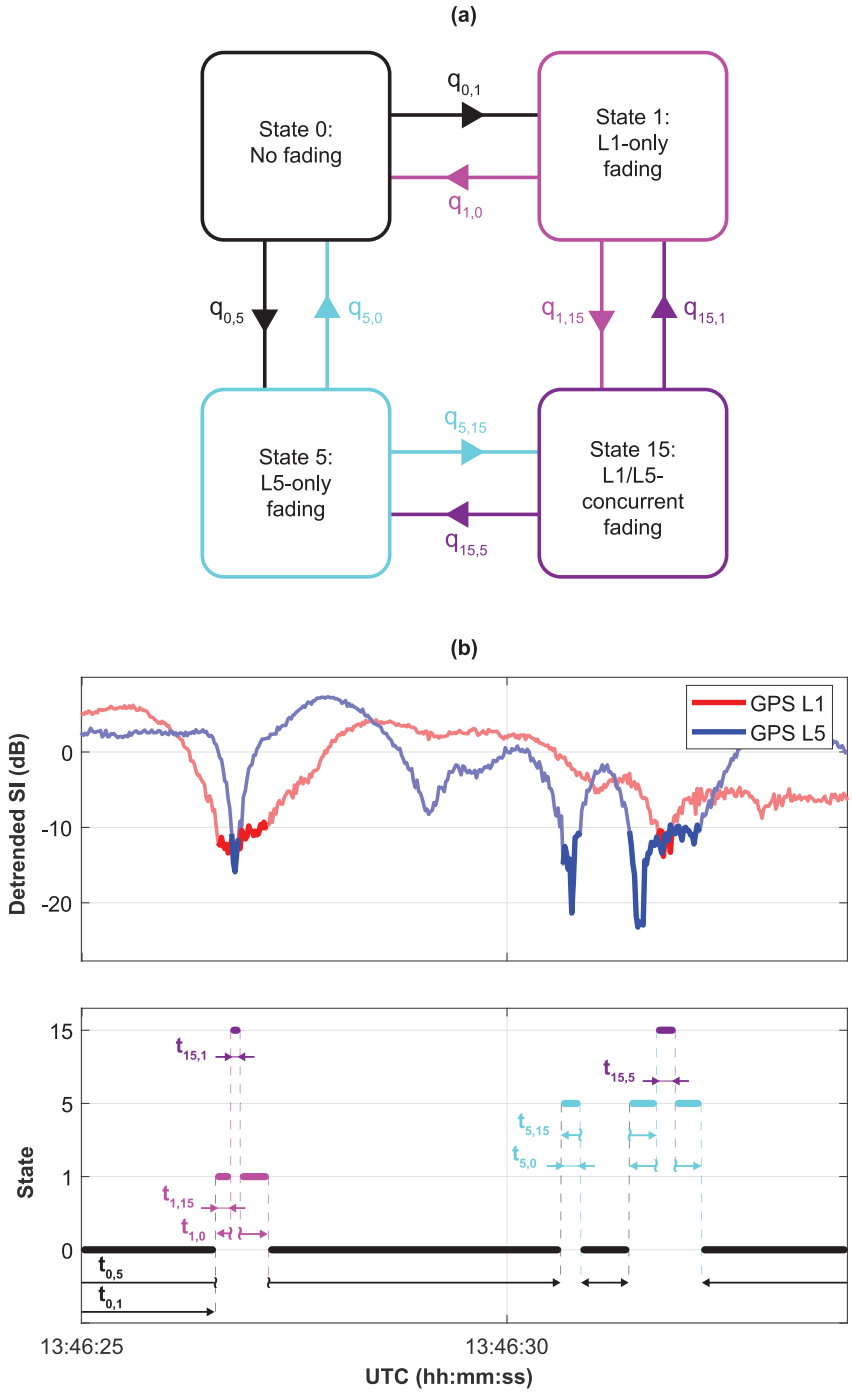

Figure 7. Markov chain-based fading process model for dual-frequency channels. (a) State-space diagram for fading processes in dual-frequency channels. States 0, 1, 5, and 15 correspond to no fading, L1-only fading, L5-only fading, and L1/L5-concurrent fading, respectively. The transition rate from state i to j is given by $q_{i,j}$ which can be estimated by the reciprocal of the mean times to state transitions. (b) An example of measuring times to state transitions of fading processes for the Markov chain-based model.

$$P_{i,j}\left(\Delta t\right) = q_{i,j}\Delta t + h\left(\Delta t^2\right) \forall i, j \; s.t. i \neq j \tag{6}$$

$$P_{i,i}\left(\Delta t\right) = 1 - q_{i,i}\Delta t + h\left(\Delta t^2\right) where \; q_{i,i} \equiv \sum_{j,j\neq i} q_{i,j} \tag{7}$$

where $h\left(\Delta t^2\right)$ indicates higher order terms which can be neglected for small Δt (a sampling rate of 50 Hz and a corresponding time step Δt of 0.02 s were used for both modeling and simulation in this study). Therefore, based on Equations 6 and 7, the transition probability matrix $P\left(\Delta t\right)$ of the Markov chain-based fading process model for dual-frequency channels can be represented as

$$\mathrm{P}\left(\Delta t\right) = \begin{bmatrix} 1-\left(q_{0,1}+q_{0,5}\right)\Delta t & q_{0,1}\Delta t & q_{0,5}\Delta t & 0 \\ q_{1,0}\Delta t & 1-\left(q_{1,0}+q_{1,15}\right)\Delta t & 0 & q_{1,15}\Delta t \\ q_{5,0}\Delta t & 0 & 1-\left(q_{5,0}+q_{5,15}\right)\Delta t & q_{5,15}\Delta t \\ 0 & q_{15,1}\Delta t & q_{15,5}\Delta t & 1-\left(q_{15,1}+q_{15,5}\right)\Delta t \end{bmatrix} \tag{8}$$

The transition rates were estimated from the observed fading processes of the March 2, 2014 Hong Kong data set presented in Section 2. Figure 7b shows an example of measuring time to state transition $t_{i,j}$ from starting state i to ending state j as observed in the data set. Note that the time to state transition $t_{i,j}$ is not a direct time interval between transitions from state i to j, but the time residing in state i until the following transition from state i to j. For example, in Figure 7b, $t_{1,0}$ is measured from the time residing in state 1 until the following transition from state 1 to state 0, and the duration of state 15 is not counted in this duration, $t_{1,0}$.

Transitions from lower states to upper states represent *time to fade*, which is the time measured under the starting state until the following ending state when the intensity of L1 or L5 signal fades below the threshold. For example, $t_{0,1}$ is the time residing in state 0 (no fading) until the following L1 fading onset, and $t_{0,5}$ is the time residing in state 0 until the following L5 fading onset. Transitions from upper states to lower states represent *fading duration*, which is the time measured under the starting state until the following ending state when the intensity of L1 or L5 signal recovers from fades. For example, $t_{1,0}$ is the time residing in state 1 (L1-only fading) until the following L1 signal recovery from fading, and $t_{5,0}$ is the time residing in state 5 (L5-only fading) until the following L5 signal recovery from fading. Both time intervals are related to the fading characteristics explained in Section 3.2, while the time between fading onsets includes fading duration and time to fade for each fading event. Each transition rate $q_{i,j}$ is estimated by the reciprocal of the mean time interval $t_{i,j}$ by fitting it into the corresponding exponential distribution.

An important implication of this model is that state transitions of the fading processes can be described as conditional probabilities depending on the current state. If deep fades between two different channels are correlated, then the model will have different probabilities for occurrences of a certain event (for example, $q_{0,1}$ and $q_{5,15}$ for L1 fading) depending on the states that fading processes transit from (state 0 and 5). This allows the Markov chain-based model to generate correlated fading processes that result in more frequent or less frequent concurrent deep fades compared to those generated by independent fading channels. Hence, this model enables simulation of correlated deep fades between L1 and L5 frequency channels by designating individual rates for all possible state transitions.

Figure 8 shows normalized histograms of all possible times to state transitions of fading processes in the GPS L1 and L5 dual-frequency channels. These normalized histograms were fitted into exponential distributions with corresponding rates to derive parameters for the Markov chain-based model proposed in this paper. Interestingly, we observed a larger transition rate (i.e., transition probability) due to L1 fading onsets given state 5 (L5-only fading), $q_{5,15}$ (shown in Figure 8b), compared to state 0 (no fading), $q_{0,1}$ (shown in Figure 8a). The same observation was made for the transition due to L5 fading onsets, where $q_{1,15}$ (shown in Figure 8d) is larger than $q_{0,5}$ (shown in Figure 8c). This indicates that, as expected, deep fades in L1/L5 dual-frequency channels are observed to be positively correlated in the March 2, 2014 Hong Kong data set. In other words, L1 fading is more likely to occur when L5-only fading is already present compared to when no fades are present, and L5 fading occurs in the same manner. However,

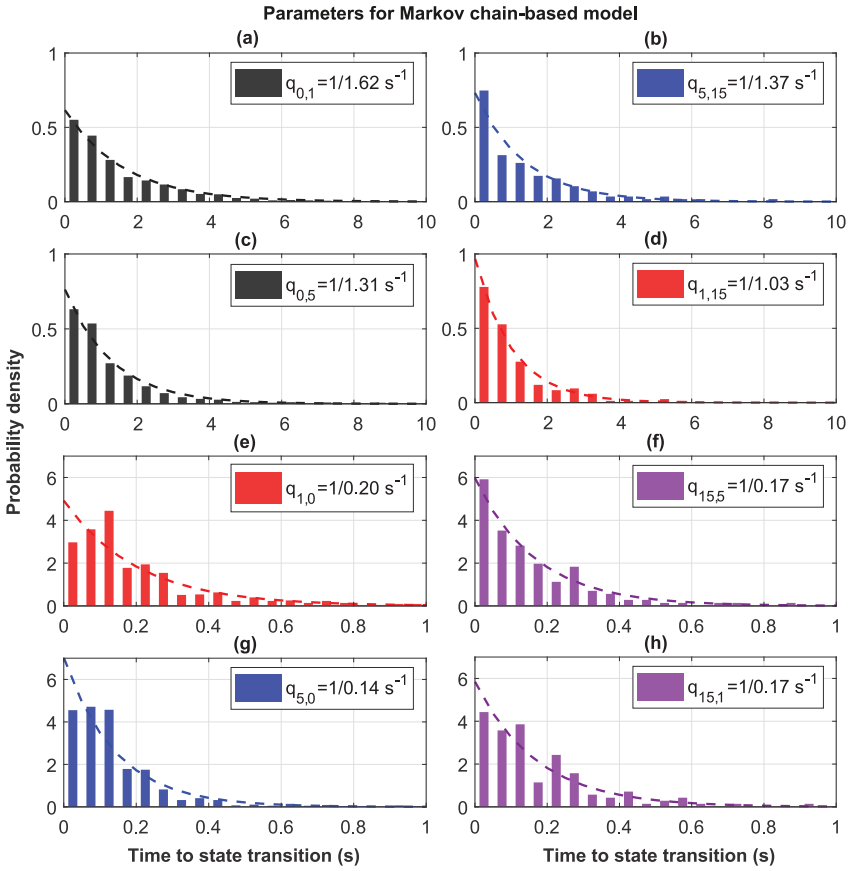

Figure 8. Normalized histograms of all times to state transitions for fading processes in Global Positioning System (GPS) L1 and L5 channels as described in Figure 7b. The normalized histograms are fitted into exponential distributions with corresponding rates, which are parameters for the Markov chain-based model. (a) and (b) Histograms of times to state transition due to L1 fading onsets given state 0 (no fading) and state 5 (L5-only fading). (c) and (d) Histograms of times to state transition due to L5 fading onsets given state 0 (no fading) and state 1 (L1-only fading). (e) and (f) Histograms of times to state transition due to L1 signal recovery given state 1 (L1-only fading) and state 15 (L1/L5-concurrent fading). (g) and (h) Histograms of times to state transition due to L5 signal recovery given state 5 (L5-only fading) and state 15 (L1/L5-concurrent fading).

there is no significant difference between transition rates for L1 and L5 signal recovery from fades depending on the starting state; thus it is hard to say whether L1 and L5 fading durations are also positively correlated.

4.3. Characteristics of Real and Simulated Fading Processes

To evaluate the statistical accuracy of the fading process models described in Sections 4.1 and 4.2, fading processes were simulated with a time step Δt of 0.02 s over a period of 10^6 seconds to obtain fully converged empirical statistics of deep fading. Figure 9 compares the normalized histograms of the deep fading characteristics extracted from the real data from Hong Kong, simulated data from the Poisson process-based model in Sun et al. (2020), and simulated data from the Markov chain-based model proposed in Section 4.2. The results show comparable statistics of deep fading characteristics between the real data and the simulated data from the Markov chain-based model. It is noteworthy that the distributions of L1/L5-concurrent fading characteristics from the Markov chain-based model are very similar to those of the real data (shown in Figures 9e and 9f), which indicates that this model more accurately describes the actual behavior of the correlated fading processes by accounting for interdependencies across frequency bands. Compared to the Markov chain-based model, the Poisson process-based model has different distributions of deep fading characteristics compared to the real data. The Poisson process-based model generates less frequent but

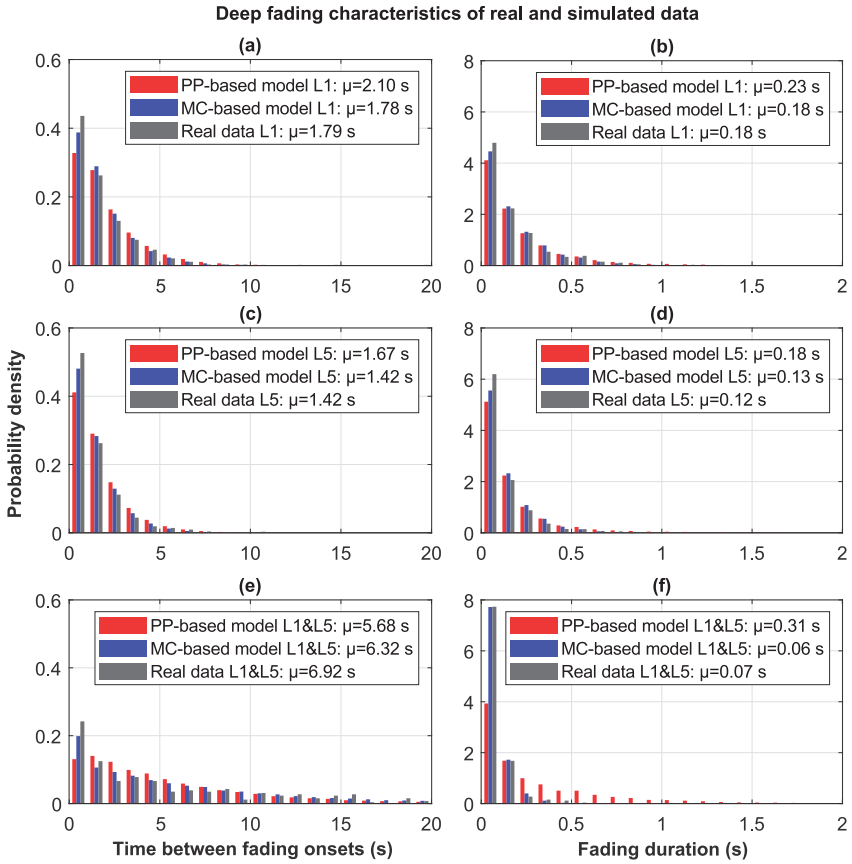

Figure 9. Normalized histograms of deep fading characteristics: Time between fading onsets and fading duration for (a) and (b) Global Positioning System (GPS) L1 (c) and (d) L5 and (e) and (f) L1/L5-concurrent deep fading. Deep fading characteristics from the Poisson process-based model (red), Markov chain-based model (blue), and Hong Kong data (gray) were compared with their mean values.

longer fades for both L1 and L5 deep fading, and more frequent but also longer fades for L1/L5-concurrent deep fading.

Table 1 summarizes the results of fading process generation from the Poisson process-based and Markov chain-based models by comparing the percentage of time spent in GPS L1 deep fading, L5 deep fading, and L1/L5-concurrent deep fading states in the Hong Kong data set to the simulation results from these models. Results from the Poisson process-based model have significantly higher percentages of all types of deep fading, in particular for L1/L5-concurrent deep fading: 5.87% for the Poisson process-based model in contrast to 1.31% for the Hong Kong data set. In contrast, the Markov chain-based model generated deep fades with very similar percentages to those of the real scintillation data (e.g., 1.35% for L1/L5-concurrent deep fading).

Table 1
The Percentage of GPS L1, L5, and L1/L5-Concurrent Deep Fading Over Time Observed in the Hong Kong Data Set Compared to That Simulated in the Poisson Process-Based and Markov Chain-Based Models

	L1 Fading	L5 Fading	L1/L5-Concurrent fading
Hong Kong data set	11.00%	10.16%	1.31%
Poisson process-based model	11.87%	12.10%	5.87%
Markov chain-based model	11.09%	10.28%	1.35%

5. Availability Analysis Under Strong Scintillation

5.1. Availability Simulation Procedure

This section analyzes the availability of GNSS-based aviation applications under a strong scintillation scenario. We assumed a conservative scenario in which all satellites in view (rather than only those in one sector of the sky, as is typically the case) experience deep fades generated by the proposed Markov chain-based model introduced in Section 4.2. Possible signal outages were assumed to occur due to deep fading according to two parameters: *Mean time to loss of lock* (under deep fading) and *mean time to reacquisition* (following loss of lock). As the counting process of signal

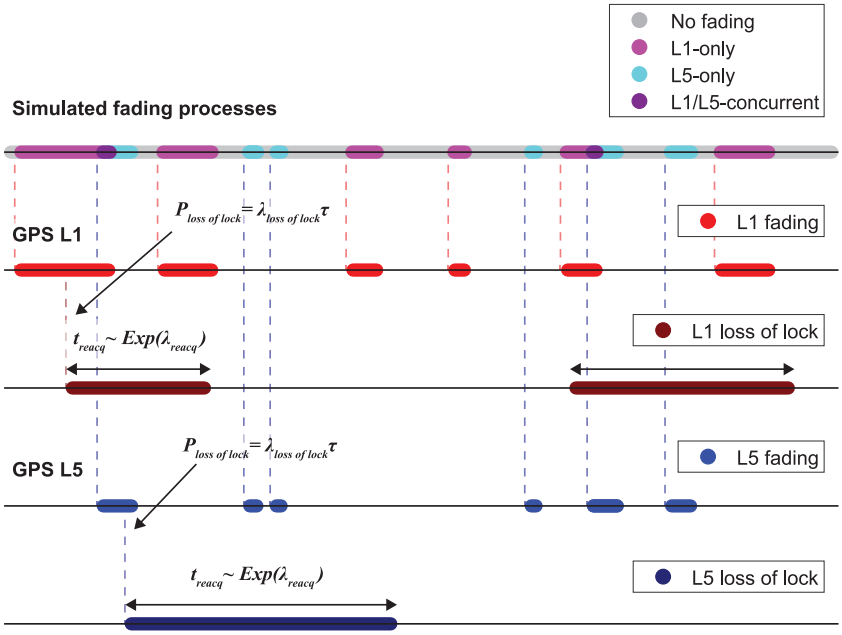

Figure 10. An example of deep fades and resultant losses of lock of Global Positioning System (GPS) L1/L5 dual-frequency channels with mean time to loss of lock set to 0.6 s and mean time to reacquisition set to 1 s.

loss (or cycle slip) can be assumed to follow a Poisson distribution (Knight, 2000), the probability of signal loss in τ s under the period of deep fading is approximately given by

$$P_{loss\ of\ lock} = \lambda_{loss\ of\ lock}\tau \tag{9}$$

where $\lambda_{\text{loss of lock}}$ is the Poisson rate parameter of signal loss, which is the reciprocal of the mean time to loss of lock. Similarly, the reacquisition process can be also modeled as a Poisson distribution. The arrival time of the reacquisition can be generated from the corresponding exponential distribution with the rate parameter given by the reciprocal of the mean time to reacquisition. The reacquisition time follows signal recovery after a given fading duration, provided that loss of lock occurs under deep fading. Since the mean time to loss of lock and mean time to reacquisition are a function of receiver tracking specifications, both parameters were parametrically analyzed (from 0 to 2 s with step size of 0.2 s for both) to cover a range of receiver performance characteristics.

Figure 10 shows an example of deep fades and the resultant losses of lock (randomly sampled with Poisson distributions of time to loss of lock and time to reacquisition) that feeds the availability simulation to apply the scintillation effects.

The Matlab Algorithm Availability Simulation Tool (MAAST) (Jan et al., 2009) was modified to incorporate the scintillation effects from losses of lock due to deep fades generated by the Markov chain-based fading process model (presented in Section 4.2). The impact of scintillation on aviation availability was considered in two ways. First, satellite geometry loss during signal tracking outages was considered because lost satellite signals cannot be used for receiver position and time calculations. In addition, loss of lock caused by scintillation can lead to shorter carrier smoothing time intervals and higher protection levels due to increased pseudorange measurement noise. Most GNSS-based aviation applications use a Hatch filter to lower the noise level of pseudorange measurements by smoothing. Frequent loss of lock reduces the effective smoothing time, leading to consistently higher noise levels on pseudorange measurements. The relative noise level on pseudorange measurements with respect to the fully converged value is modeled as,

$$Relative\ noise\ level = 1 + 9e^{\frac{-\tau}{100}} \tag{10}$$

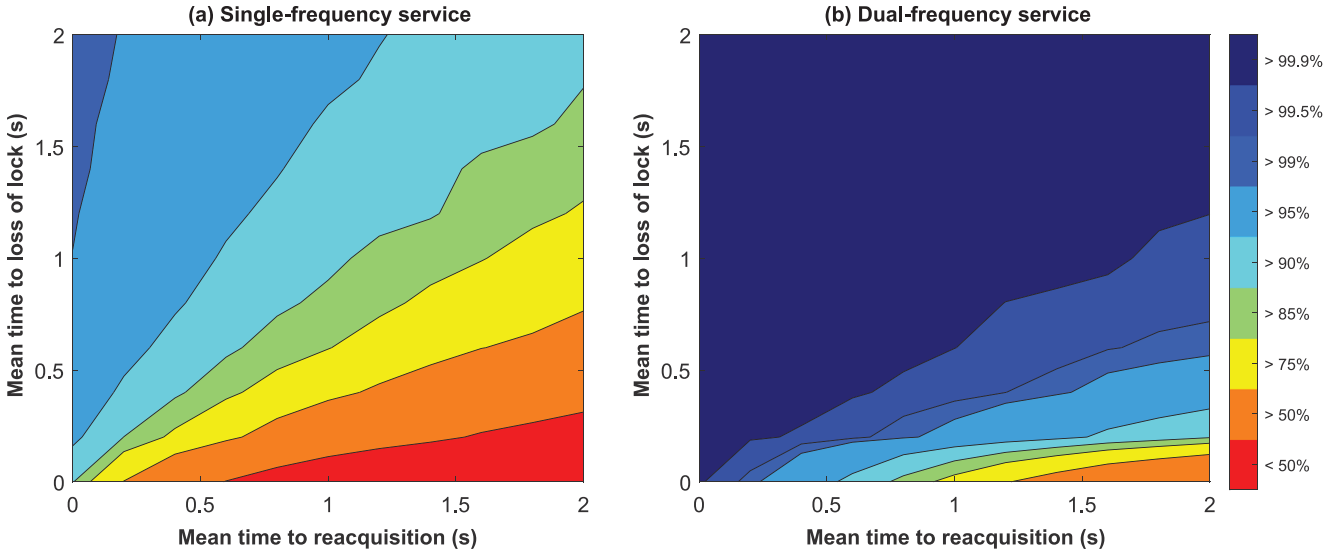

Figure 11. LPV-200 availability simulation results under a strong scintillation scenario with GIVEI of 11 for the aviation operation of (a) Global Positioning System (GPS) L1 single-frequency and (b) L1/L5 dual-frequency services.

where τ is the time in seconds after filter reset (τ begins once a lost satellite is reacquired and smoothing restarts) (Seo et al., 2011a). This model is based on the observation that the smoothing would result in a reduction in the noise level by as high as a factor of 10 (Murphy et al., 2005). The time constant of the Hatch filter was set to 100 s, as specified in the Wide Area Augmentation System (WAAS) Minimum Operational Performance Standards (MOPS) (RTCA, 2020).

The availability studies in this paper assumed the use of a satellite based augmentation system (SBAS) similar to WAAS that supports the localizer performance with vertical guidance (LPV)-200 requiring high levels of integrity and availability. Availability was calculated as the percentage of operational time for which the vertical protection level (VPL) is lower than the vertical alert limit (VAL) of 35 m for the LPV-200 operation. VPLs were calculated based on the broadcast integrity parameters and error models which provide uncertainty of corrections for each error source. A 1 m of user differential range error (UDRE), which is the bounded standard deviation of remaining satellite clock and ephemeris errors after applying differential corrections, was used to determine VPLs. The uncertainty on ionospheric corrections for single-frequency SBAS was based on a grid ionospheric vertical error indicator (GIVEI), a confidence bound on the estimation error of the vertical ionospheric delay at each ionospheric grid point. In this study, constant GIVEIs ranging from 5 (1.8 m, 99.9%) to 11 (4.5 m, 99.9%) were assumed for all ionospheric pierce points of GPS satellites. In the case of dual-frequency service, the ionosphere-free dual-frequency code noise/multipath model was used. Moreover, a loss of one frequency in the dual-frequency service resulted in the use of the GIVEI for the single-frequency service to support temporary single-frequency operations. The contributions of residual tropospheric delay and airborne code noise/multipath errors were included by using their respective error models in WAAS MOPS (RTCA, 2020). VPLs for a single static user in Hong Kong were calculated every second for a 6-h period nearly after sunset (from 19:00:00 to 25:00:00 LT), when the effects of scintillation are the most severe in the equatorial region. During the period, the scenario employed the GPS ephemeris data with a visibility mask angle of 5° on March 2, 2014 (akin to the Hong Kong data set).

5.2. Availability Simulation Results

Figure 11 shows the availability results for LPV-200 under a strong scintillation scenario with GIVEI set to 11. The simulations were performed parametrically based on the two parameters which depend on receiver tracking performance: *Mean time to loss of lock* and *mean time to reacquisition*. The availability contour plots in Figure 11 show a significant availability improvement using dual-frequency signals (shown in Figures 11b) compared to the existing single-frequency service (shown in Figures 11a) for all combinations of receiver tracking parameters. For example, single-frequency service requires immediate reacquisition of

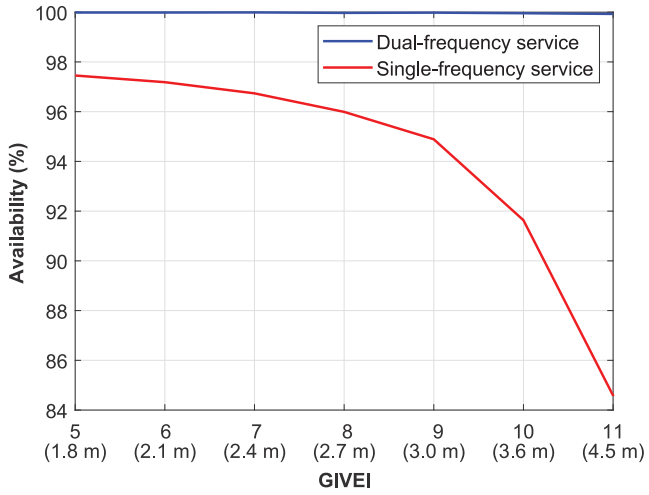

Figure 12. Availability of Global Positioning System (GPS) L1 single and L1/L5 dual-frequency services according to GIVEI with mean time to loss of lock set to 0.6 s and mean time to reacquisition set to 1 s.

receiver signal tracking to provide 95% availability when the mean time to loss of lock is 0.6 s, whereas reacquisition within 1 s is sufficient to provide over 99.9% availability for dual-frequency service.

An availability analysis while varying GIVEI was also conducted to investigate the sensitivity of availability to ionospheric correction errors for single-frequency SBAS. Ionospheric correction errors are likely to increase with significant scintillation because electron density irregularities reduce the spatial consistency of ionospheric delays (Lee et al., 2017; Yoon et al., 2017), resulting in a degradation of the quality of delay estimation by SBAS ground station networks. Figure 12 shows almost consistent near-100% availability of the dual-frequency service as a function of GIVEI (minimum 99.93% for GIVEI of 11), whereas that of the single-frequency service is greatly reduced as GIVEI increases. This sensitivity study shows that the availability benefit of dual-frequency SBAS service increases as ionospheric correction errors increase under the influence of strong scintillation. These results were expected because dual-frequency SBAS directly corrects for ionospheric delays and is not sensitive to GIVEI except when the loss of a satellite on one of the two frequencies causes a temporary downgrade to single-frequency SBAS for that satellite. More accurate sensitivity analysis could be made by estimating actual GIVEI values over SBAS service areas instead of constant GIVEI values over large regions.

Although the availability results in Figures 11 and 12 are only based on the characteristics of the March 2, 2014 Hong Kong scintillation data set, analysis of additional datasets using the Markov chain-based modeling approach of Section 4.2 will enable the simulation tool to provide availability estimates under various levels of scintillation severity. More comprehensive analyses of this type will make it possible to recommend receiver performance standards and mitigation strategies for aviation during strong scintillation.

6. Conclusions and Future Work

This paper has proposed a new stochastic model for correlated signal fading processes to better model the impact of strong ionospheric scintillation and to evaluate the availability of dual-frequency GNSS-based applications under scintillation. Correlated deep fading processes between the L1 and L5 frequency channels were analyzed and characterized from a data set collected during a strong scintillation period in Hong Kong in March 2, 2014 to provide inputs to a Markov chain-based model. The proposed model describes fading processes with conditional probabilities (based on Poisson rate parameters) of transitions for all possible fading states in which dual-frequency signals for a single satellite can reside. The temporal correlation between fading channels is considered by allowing different parameters for each transition (fading or recovery) depending on the current (pre-transition) fading state to provide an accurate description of fading processes in real scintillation data.

A statistical study of deep fading characteristics was conducted by comparing the Poisson process-based model in Sun et al. (2020) and the Markov chain-based model with the actual behavior in the March 2, 2014 Hong Kong data set. The statistics and histograms of *time between fading onsets* and *fading duration* for GPS L1, L5, and L1/L5-concurrent deep fades generated from the Markov chain-based model are very similar to those of the Hong Kong data set, while the Poisson process-based model generates much longer deep fades for all three types of deep fading. Moreover, the accurately modeled percentage of deep fading over time (in particular for L1/L5-concurrent deep fading) confirms that the Markov chain-based model can emulate the actual behavior of correlated fading processes across frequency bands under strong scintillation.

To investigate the variability of the system-level impact of deep fading, availability simulations were parametrically conducted while varying mean time to loss of lock and mean time to reacquisition, both of which depend on GNSS receiver tracking performance. LPV-200 aircraft approach availability results under the scintillation effects generated by the proposed model demonstrated a significant availability benefit from

(near-future) dual-frequency SBAS compared to the existing single-frequency SBAS for every combination of these two parameters. This parametric analysis confirmed that, as expected, aviation availability during strong scintillation is significantly enhanced with the use of dual-frequency signals, and it is very sensitive to both mean time to loss of lock and mean time to reacquisition. Furthermore, a sensitivity study based on varying ionospheric correction error bounds as expressed by GIVEI (for single-frequency SBAS operations) shows that the ionospheric correction error also has a significant impact on aviation availability under scintillation. Because dual-frequency SBAS availability is mostly independent of the value of GIVEI that can be supported by single-frequency SBAS, a larger availability benefit can be obtained from dual-frequency SBAS when single-frequency SBAS is affected by higher GIVEI, especially when ionospheric irregularities (e.g., EPBs) reduce the spatial consistency of ionospheric delays.

Information regarding SBAS single-frequency ionospheric correction errors (GIVEI values) during strong scintillation is needed to obtain more specific availability simulation results. Strong scintillation is very rare in the mid-latitude regions covered by existing SBAS systems such as WAAS and European Geostationary Navigation Overlay Service (EGNOS), but it may be possible to simulate single-frequency SBAS algorithms with real data collected during scintillation conditions to estimate typical GIVEI values under scintillation.

This paper used a single data set of strong scintillation (S_4 index around or exceeding unity) to show an availability benefit from dual-frequency service. The data set only represents a specific scintillation condition, and thus cannot cover a full range of scintillation conditions. Broader and more useful availability results can be obtained by using datasets representing varied scintillation conditions depending on satellite-receiver geometries and diurnal, seasonal, annual, and longitudinal variations of EPBs. Fading process models representing a variety of scintillation conditions should be used to re-evaluate aviation availability to provide performance standards and mitigation strategies for GNSS under strong (but varied) scintillation conditions.

The receiver tracking performance parameters varied in this study, mean time to loss of lock and mean time to reacquisition, can be approximately modeled as a function of receiver tracking loop design (e.g., bandwidth, loop order, and discriminator type) and tracking conditions (e.g., carrier to noise ratio). Hence, further analysis of the relationship between the receiver tracking parameters and receiver design specifications will help us propose updated performance standards for aviation receivers to further reduce the impacts of strong scintillation.

This paper focuses on the scintillation effects in equatorial region where strong amplitude scintillation with frequent and deep signal fading tends to occur. In contrast, phase scintillation with abrupt phase fluctuations is observed to be dominant in high-latitude region (Jiao & Morton, 2015). Therefore, new approaches would be required to extend this work to the modeling of high-latitude scintillation characteristics.

The proposed fading process model can be applied to various GNSS-based architectures. In particular, we are looking forward to extending this approach to multi-constellation and multi-frequency systems. The Markov chain-based model enables more realistic availability assessment of these systems because it can easily be expanded to generate realistically correlated fading processes across multiple frequency bands and multiple satellite types, as demonstrated in this paper for a GPS-only dual-frequency example.

Acknowledgments
Andrew Kiyoung Sun was supported by the National Research Foundation of Korea (NRF) grant funded by the Korea government (MSIT) (No. NRF-2019M1A3B2A0410271412). Hyeyeon Chang was supported by the MSIT (Ministry of Science, ICT), Korea, under the High-Potential Individuals Global Training Program (No. 2019-0-01598) supervised by the IITP (Institute for Information & Communications Technology Planning & Evaluation). Hyosub Kil in JHU/APL acknowledges the support by NSF-AGS2029840 and AFOSR. The Hong Kong data set used in this study was collected by a system built at the Satellite Navigation and Sensing Lab at the University of Colorado Boulder and hosted by Prof. Zhizhao Liu from Hong Kong Polytechnic University.

Data Availability Statement

The Hong Kong data set used in this study is available from https://github.com/cu-sense-lab/gnss-scintillation-simulator/tree/master/example-data (see readme.md file in the repository for the data outlines). The DMSP-SSUSI (SDR2 data product) and C/NOFS-CINDI data are available from the Johns Hopkins University Applied Physics Laboratory SSUSI website (https://ssusi.jhuapl.edu/data_products) and NASA's heliophysics data portal (https://heliophysicsdata.gsfc.nasa.gov/websearch/dispatcher), respectively.

References

Basu, S., Groves, K. M., Basu, S., & Sultan, P. J. (2002). Specification and forecasting of scintillations in communication/navigation links: Current status and future plans. *Journal of Atmospheric and Solar-Terrestrial Physics*, *64*(16), 1745–1754. https://doi.org/10.1016/S1364-6826(02)00124-4

Basu, S., MacKenzie, E., & Basu, S. (1988). Ionospheric constraints on VHF/UHF communications links during solar maximum and minimum periods. *Radio Science*, *23*(3), 363–378. https://doi.org/10.1029/RS023i003p00363

Billinton, R., & Allan, R. N. (1983). *Reliability evaluation of engineering systems: Concepts and techniques*. Springer. https://doi.org/10.1007/978-1-4899-0685-4

Breitsch, B., Morton, Y. T., Rino, C., & Xu, D. (2020). GNSS carrier phase cycle slips due to diffractive ionosphere scintillation: Simulation and characterization. *IEEE Transactions on Aerospace and Electronic Systems*, *56*(5), 3632–3644. https://doi.org/10.1109/TAES.2020.2979025

Carrano, C. S., Groves, K. M., McNeil, W. J., & Doherty, P. H. (2012). *Scintillation characteristics across the GPS frequency band*. Paper presented at 25th International Technical Meeting of the Satellite Division of The Institute of Navigation (ION GNSS 2012).

FAA (2010). *Phase II of the GNSS evolutionary architecture study*. https://www.faa.gov/about/office_org/headquarters_offices/ato/service_units/techops/navservices/gnss/library/documents/media/GEASPhaseII_Final.pdf

Fejer, B. G., Scherliess, L., & de Paula, E. R. (1999). Effects of the vertical plasma drift velocity on the generation and evolution of equatorial spread F. *Journal of Geophysical Research*, *104*(A9), 19859–19869. https://doi.org/10.1029/1999JA900271

Felux, M., Circiu, M. S., Lee, J., & Holzapfel, F. (2017). Ionospheric gradient threat mitigation in future dual frequency GBAS. *International Journal of Aerospace Engineering*, *2017*, 4326018. https://doi.org/10.1155/2017/4326018

Gallager, R. G. (1996). *Discrete stochastic processes*. Springer.

Gerbeth, D., Circiu, M. S., Caamano, M., & Felux, M. (2016). Nominal performance of future dual frequency dual constellation GBAS. *International Journal of Aerospace Engineering*, *2016*, 6835282. https://doi.org/10.1155/2016/6835282

Humphreys, T. E., Psiaki, M. L., Ledvina, B. M., Cerruti, A. P., & Kintner, P. M. (2010). Data-driven testbed for evaluating GPS carrier tracking loops in ionospheric scintillation. *IEEE Transactions on Aerospace and Electronic Systems*, *46*(4), 1609–1623. https://doi.org/10.1109/TAES.2010.5595582

Hysell, D. L., Kelley, M. C., Swartz, W. E., & Woodman, R. F. (1990). Seeding and layering of equatorial spread F by gravity waves. *Journal of Geophysical Research: Space Physics*, *95*(A10), 17253–17260. https://doi.org/10.1029/JA095iA10p17253

ICAO (2018). *Concept of operations (CONOPS) for dual-frequency multi-constellation (DFMC) global navigation satellite system (GNSS) (ConOps v6.4)*. Retrieved from https://www.icao.int/Meetings/anconf13/Documents/WP/Navigation_Systems_Panel_CONOPS_for_DFMC_GNSS.pdf

ITU (2013). *Ionospheric propagation data and prediction methods required for the design of satellite services and systems (Recommendation ITU-R P. 531-12)*. ITU.

Jan, S., Chan, W., & Walter, T. (2009). MATLAB algorithm availability simulation tool. *GPS Solutions*, *13*, 327–332. https://doi.org/10.1007/s10291-009-0117-4

Jiao, Y., Morton, Y., Akos, D., & Walter, T. (2015). A Comparative study of triple frequency GPS scintillation signal amplitude fading characteristics at low latitudes. Paper presented at 28th International Technical Meeting of the Satellite Division of The Institute of Navigation (ION GNSS+ 2015).

Jiao, Y., & Morton, Y. T. (2015). Comparison of the effect of high-latitude and equatorial ionospheric scintillation on GPS signals during the maximum of solar cycle 24. *Radio Science*, *50*(9), 886–903. https://doi.org/10.1002/2015RS005719

Jiao, Y., Xu, D., Morton, Y., & Rino, C. (2016). Equatorial scintillation amplitude fading characteristics across the GPS frequency bands. *Journal of the Institute of Navigation*, *63*(3), 267–281. https://doi.org/10.1002/navi.146

Kelley, M. C., Larsen, M. F., LaHoz, C., & McClure, J. P. (1981). Gravity wave initiation of equatorial spread F: A case study. *Journal of Geophysical Research*, *86*(A11), 9087–9100. https://doi.org/10.1029/JA086iA11p09087

Kelley, M. C., Makela, J. J., Paxton, L. J., Kamalabadi, F., Comberiate, J. M., & Kil, H. (2003). The first coordinated ground- and space-based optical observations of equatorial plasma bubbles. *Geophysical Research Letters*, *30*(14), 1766. https://doi.org/10.1029/2003GL017301

Kil, H., Heelis, R. A., Paxton, L. J., & Oh, S. -J. (2009). Formation of a plasma depletion shell in the equatorial ionosphere. *Journal of Geophysical Research*, *114*, A11302. https://doi.org/10.1029/2009JA014369

Kintner, P. M., Ledvina, B. M., & de Paula, E. R. (2007). GPS and ionospheric scintillations. *Space Weather*, *5*, S09003. https://doi.org/10.1029/2006SW000260

Knight, M. (2000). *Ionospheric scintillation Effects on global positioning system receivers (Doctoral dissertation)*. University of Adelaide. https://digital.library.adelaide.edu.au/dspace/bitstream/2440/19809/2/02whole.pdf

Lee, J., Morton, Y. T. J., Lee, J., Moon, H., & Seo, J. (2017). Monitoring and mitigation of ionospheric anomalies for GNSS-based safety critical systems: A review of up-to-date signal processing techniques. *IEEE Signal Processing Magazine*, *34*(5), 96–110. https://doi.org/10.1109/MSP.2017.2716406

Morton, Y., Jiao, Y., Van Graas, F., Vinande, E., & Pujara, N. (2015). *Analysis of receiver multi-frequency response to ionospheric scintillation in ascension Island, Hong Kong, and Singapore*. Paper presented at ION 2015 Pacific PNT Meeting.

Murphy, T., Matt, H., Geren, P., Pankaskie, T., Clark, B., & Burns, J. (2005). *More results from the investigation of airborne multipath errors*. Paper presented at the 18th International Technical Meeting of the Satellite Division of The Institute of Navigation (ION GNSS 2005).

Ogawa, T., Sinno, K., Fujita, M., & Awaka, J. (1980). Severe disturbances of VHF and GHz waves from geostationary satellites during a magnetic storm. *Journal of Atmospheric and Terrestrial Physics*, *42*(7), 637–644. https://doi.org/10.1016/0021-9169(80)90098-7

Ott, E. (1978). Theory of Rayleigh-Taylor bubbles in the equatorial ionosphere. *Journal of Geophysical Research: Space Physics*, *83*(A5), 2066–2070. https://doi.org/10.1029/JA083iA05p02066

Paxton, L. J., Schaefer, R. K., Zhang, Y., & Kil, H. (2017). Far ultraviolet instrument technology. *Journal of Geophysical Research: Space Physics*, *122*(2), 2706–2733. https://doi.org/10.1002/2016JA023578

RTCA (2020). *Minimum operational performance standards (MOPS) for global positioning system/satellite-based augmentation system Airborne equipment (DO-229)*. RTCA, Inc.

Seo, J., & Walter, T. (2014). Future dual-frequency gps navigation system for intelligent air transportation under strong ionospheric scintillation. *IEEE Transactions on Intelligent Transportation Systems*, *15*(5), 2224–2236. https://doi.org/10.1109/TITS.2014.2311590

Seo, J., Walter, T., Chiou, T. -Y., & Enge, P. (2009). Characteristics of deep GPS signal fading due to ionospheric scintillation for aviation receiver design. *Radio Science*, *44*, RS0A16. https://doi.org/10.1029/2008RS004077

Seo, J., Walter, T., & Enge, P. (2011a). Availability impact on GPS aviation due to strong ionospheric scintillation. *IEEE Transactions on Aerospace and Electronic Systems*, *47*(3), 1963–1973. https://doi.org/10.1109/TAES.2011.5937276

Seo, J., Walter, T., & Enge, P. (2011b). Correlation of GPS signal fades due to ionospheric scintillation for aviation applications. *Advances in Space Research*, *47*(10), 1777–1788. https://doi.org/10.1016/j.asr.2010.07.014

Skone, S., Knudsen, K., & de Jong, M. (2001). Limitations in GPS receiver tracking performance under ionospheric scintillation conditions. *Physics and Chemistry of the Earth - Part A*, *26*(6–8), 613–621. https://doi.org/10.1016/S1464-1895(01)00110-7

Sun, K., Chang, H., Lee, J., Seo, J., Morton, Y. J., & Pullen, S. (2020). *Performance benefit from dual-frequency GNSS-based aviation applications under ionospheric scintillation: A new approach to fading process modeling*. Meeting of The Institute of Navigation. https://doi.org/10.33012/2020.17184

Van Dierendonck, A. J., & Arbesser-Rastburg, B. (2004). *Measuring ionospheric scintillation in the equatorial region over Africa, including measurements from SBAS Geostationary satellite signals*. Paper presented at 17th International Technical Meeting of the Satellite Division of The Institute of Navigation (ION GNSS 2004).

Van Dierendonck, A. J., Klobuchar, J., & Hua, Q. (1993). *Ionospheric scintillation monitoring using Commercial single frequency C/A code receivers*. Paper presented at 6th International Technical Meeting of the Satellite Division of The Institute of Navigation (ION GPS 1993).

Walter, T., Blanch, J., Eric Phelts, R., & Enge, P. (2012). Evolving WAAS to Serve L1/L5 Users. *Navigation*, *59*(4), 317–327. https://doi.org/10.1002/navi.21

Woodman, R. F. (1970). Vertical drift velocities and east-west electric fields at the magnetic equator. *Journal of Geophysical Research*, *75*(31), 6249–6259. https://doi.org/10.1029/JA075i031p06249

Yeh, K. C., & Liu, C. –H. (1982). Radio wave scintillations in the ionosphere. *Proceedings of the IEEE*, *70*(4), 324–360. https://doi.org/10.1109/PROC.1982.12313

Yoon, M., Kim, D., & Lee, J. (2017). Validation of ionospheric spatial decorrelation observed during equatorial plasma bubble events. *IEEE Transactions on Geoscience and Remote Sensing*, *55*(1), 261–271. https://doi.org/10.1109/TGRS.2016.2604861